

# Multi-Label Classification of Thoracic Diseases using Dense Convolutional Network on Chest Radiographs

Dipkamal Bhusal<sup>a</sup> and Sanjeeb Prasad Panday<sup>a</sup>

<sup>a</sup>Department of Electronics and Computer Engineering, Institute of Engineering, Pulchowk Campus, Lalitpur, Nepal

## ARTICLE HISTORY

Compiled May 9, 2023

## ABSTRACT

Traditional methods of identifying pathologies in X-ray images rely heavily on skilled human interpretation and are often time-consuming. The advent of deep learning techniques has enabled the development of automated disease diagnosis systems, but the performance of such systems is dependent on the quality of the model and the level of interpretability it provides. In this paper, we propose a multi-label disease diagnosis model for chest X-rays using a dense convolutional neural network (DenseNet) and model interpretability using GRADCAM. We trained our model using frontal X-rays and evaluated its performance using various quantitative metrics, including the area under the receiver operating characteristic curve (AUC). Our proposed model achieved the highest AUC score of 0.896 for the condition Cardiomegaly with an accuracy of 0.826, while the lowest AUC score was obtained for Nodule, at 0.655 with an accuracy of 0.66. To promote model interpretability and build trust in decision making, we generated heatmaps on X-rays to visualize the regions where the model paid attention to make certain predictions. Additionally, we estimated the uncertainty in model predictions by presenting the confidence interval of our measurements. Our proposed automated disease diagnosis model obtained high performance metrics in multi-label disease diagnosis tasks and provided visualization of model predictions for model interpretability.

## KEYWORDS

deep learning; disease diagnosis; model explainability; chest x-rays

## 1. Introduction

Deep learning has revolutionized image classification by achieving remarkable improvements in performance and accuracy (Krizhevsky et al. (2012); Ren et al. (2015); Simonyan and Zisserman (2015); Szegedy et al. (2017); He et al. (2016)). The availability of large labeled datasets has enabled researchers to accurately classify and identify images, including medical images. Deep learning has shown immense potential in health analytics, particularly in automating the diagnosis process and providing faster results without the need for professional medical staff. This is especially important given that approximately 3 billion people lack access to medical imaging expertise, as reported by the World Health Organization (Litjens et al. (2017)). An automated diagnosis system can be particularly beneficial in areas where medical expertise is limited. Highly

accurate prediction models can also assist human experts and reduce errors resulting from fatigue, cognitive or perceptual bias.

Convolutional Neural Networks (CNNs) (Fukushima and Wake (1991)) are the building blocks of image classifiers, efficiently extracting and learning image features through convolution and pooling layers. AlexNet (Krizhevsky et al. (2012)) was an early CNN architecture that used multiple convolutional and fully connected layers. VGG Net (Simonyan and Zisserman (2015) improved upon AlexNet by utilizing 16 or 19 weight layers, called VGG16 and VGG19, respectively. However, stacking convolutional layers can lead to overfitting (Goodfellow et al. (2016)). To mitigate this, Inception Net (Szegedy et al. (2017)) proposed a network with multiple filter sizes on the same level to widen the network instead of making it deeper. Residual Networks (He et al. (2016)), or ResNets, utilized skip connections to jump over layers and train the model deeper. DenseNet (Huang et al. (2017)) parallelized this approach by connecting each layer to all previous and subsequent layers, solving the vanishing gradient problem in deep neural networks. Despite the topological differences in how features are transmitted across layers, all these architectures follow the same CNN principle, consisting of convolution, sub-sampling, dense, and softmax layers.

The remarkable breakthroughs achieved by deep learning architectures in computer vision have prompted researchers to apply these techniques to medical imaging. One critical task in medical imaging is accurately diagnosing the presence or absence of disease and malignancy in patient images such as X-rays or MRIs. Deep networks have significantly improved diagnosis accuracy in various applications, including the detection of diabetic retinopathy (Tymchenko et al. (2020)) and skin cancer (Li and Shen (2018)). Given the significant health threat posed by thoracic diseases, and the widespread use of chest X-rays in medical diagnosis, several research projects have explored the performance of deep learning in detecting these conditions.



**Figure 1.** A sample of fundus photo (Tymchenko et al. (2020))



**Figure 2.** A sample of skin image (Li and Shen (2018))



**Figure 3.** A sample of chest x-ray (Wang et al. (2017))

In 2015, Bar et al. (2015) proposed a convolutional neural network classifier for the classification of pathologies in chest radiographs. The authors obtained an area under the curve of 0.87-0.94 on a test set of 433 images, demonstrating the feasibility of detecting X-ray pathology using a pre-trained model (Donahue et al. (2014)). In 2017, Cicero et al. (2017) proposed a similar CNN classifier that achieved an area under the curve of 0.964 using a medium-sized dataset of 35,000 X-rays annotated by 2443 radiologists. The authors achieved an overall sensitivity and specificity of 91% using GoogleNet (Szegedy et al. (2015)). These positive results demonstrate that deep neural network architectures can successfully detect common pathologies, even with modest-sized medical datasets.

Maduskar et al. (2013) evaluated the performance of convolutional neural networks in tuberculosis detection using a small dataset of 1007 chest X-rays. The authors

experimented with pretrained and untrained versions of two architectures, AlexNet (Krizhevsky et al. (2012)) and GoogleNet (Szegedy et al. (2015)), and obtained the best performance with an ensemble of both architectures in the pretrained condition (AUC = 0.99). The pretrained models always outperformed the untrained models. Similarly, Lakhani and Sundaram (2017) compared the performance of a computer-aided tuberculosis diagnosis system (CAD4TB) with that of health professionals and found that the tuberculosis assessment of CAD4TB was comparable to that of health officers. Tests were performed on 161 subjects.

In 2016, Wang et al. (2017) proposed a weakly controlled multi-label classification and localization of thoracic diseases using deep learning on a dataset of 108,948 images with annotations for eight different diseases. They took multi-label losses into account and aimed to detect common thoracic diseases using deep learning. Although they obtained promising results, they were skeptical about using deep neural architecture in fully automated high-precision computer-aided diagnosis systems. In 2017, Rajpurkar et al. (2017) designed a deep learning model named CheXNet that used a 121-layer convolutional neural network with dense connections and batch normalization for the detection of pneumonia. The model was trained on a publicly available dataset of 100,000 chest X-ray images and outperformed the average radiologist performance. In CheXNeXt (Rajpurkar et al. (2018)), the authors evaluated a multi-label disease diagnosis model and compared its performance with that of radiologists.

In this work, we combine the 121-layer architecture of CheXNet with the multi-class classification of CheXNeXt to make diagnostic predictions on 14 different pathological conditions in chest X-rays. We also localize the parts of the chest radiograph that indicate the presence of each pathology for model interpretability. The detection of 14 different pathology conditions, including ‘Atelectasis’, ‘Cardiomegaly’, ‘Consolidation’, ‘Edema’, ‘Emphysema’, ‘Effusion’, ‘Fibrosis’, ‘Hernia’, ‘Infiltration’, ‘Mass’, ‘Nodule’, ‘Pneumothorax’, ‘Pleural Thickening’, and ‘Pneumonia’, is a multi-label classification problem. The input to the DenseNet architecture is a chest X-ray image, and the output is a label that provides the probability that each pathology is positive in the chest X-ray.

The main contributions of this paper are summarized below:

- (1) We formulate thoracic disease identification as a multi-label classification problem and detect 14 different pathological condition in chest radiographs using dense convolutional neural network. Code is available on Github<sup>1</sup>.
- (2) We perform extensive evaluation of our models and report the highest AUC score of 0.896 for condition Cardiomegaly and the lowest AUC score for Nodule, 0.655.
- (3) For model interpretability, we explain the prediction of the deep learning model using GRADCAM and generate heatmap on x-rays to visualize regions where model paid attention to make disease prediction.

Our paper is organized as follows: We begin with introduction in Section 1. In this section, we illustrate the background on deep learning for medical image classification, and discuss current works. In Section 2, we explain our methodology by discussing data, and model architecture. We illustrate all the steps of our model development and introduce evaluation criteria. In Section 3, we present our evaluation results of the proposed diagnostic model. We present quantitative results of disease diagnosis and qualitative results of model interpretation. We discuss our results in Section 4 and conclude our findings on Section 5.

---

<sup>1</sup><https://github.com/dipkamal/chestxrayclassifier>

**Table 1.** Detail annotation in the dataset<sup>a</sup>

Image	Atelectasis	Consolidation	Edema	Effusion	PatientId
015.png	0	0	0	0	8270
001.png	1	0	0	0	29855
000.png	0	0	0	0	1297
002.png	0	0	0	0	12359
001.png	0	0	0	0	17951

<sup>a</sup> All 14 pathological conditions are not displayed due to width constraint.

## 2. Methodology

### 2.1. Data

In this study, we utilized the ChestX-ray8 dataset (Wang et al. (2017)) as the primary dataset for our research. From this dataset, we randomly selected 99,000 images, each of which was annotated with labels identifying 14 distinct pathological conditions. To examine the supervised model’s generalization capabilities, we extracted a test set of 500 images. Table 1 provides a snapshot of the dataset.

### 2.2. Pre-processing

#### 2.2.1. Addressing Data Leakage

Data leakage in medical image analysis occurs when the same patient’s images are present in both the training and test sets, leading to potential bias in the deep learning model’s decision-making process (Rathore et al. (2017)). This scenario may arise when a patient undergoes multiple chest X-rays at different time intervals, and these images are included in the dataset. To address this issue, we divided the dataset at the patient level, ensuring that images from the same patient were only present in either the training or test set, but not both. This approach effectively prevents data ”leakage” between the two sets and minimizes the risk of introducing any biases into our deep learning model.

#### 2.2.2. Preparing Images

The training dataset underwent standard preprocessing methods. Normalization of the mean and standard deviation of the input data was performed to standardize the distribution. The image size was set to 320 by 320 pixels, which is a suitable dimension for the deep layer convolutional network. To enable transfer learning using the pretrained model of ImageNet (Krizhevsky et al. (2012)), the 1-channel X-ray image was converted to a 3-channel format. The test data was normalized using the statistics of the training set to ensure that the overall distribution of data during training and testing remained consistent.

#### 2.2.3. Addressing Class Imbalance

As illustrated in Figure 4, the proportion of positive cases in the dataset was significantly lower than that of negative cases. For instance, in the case of Hernia, the ratio of positive to negative cases was only approximately 0.02, where a positive case denotes an image with a disease and a negative case denotes an image without a disease. Similarly, for Infiltration, which had the highest number of positive labels, the ratio

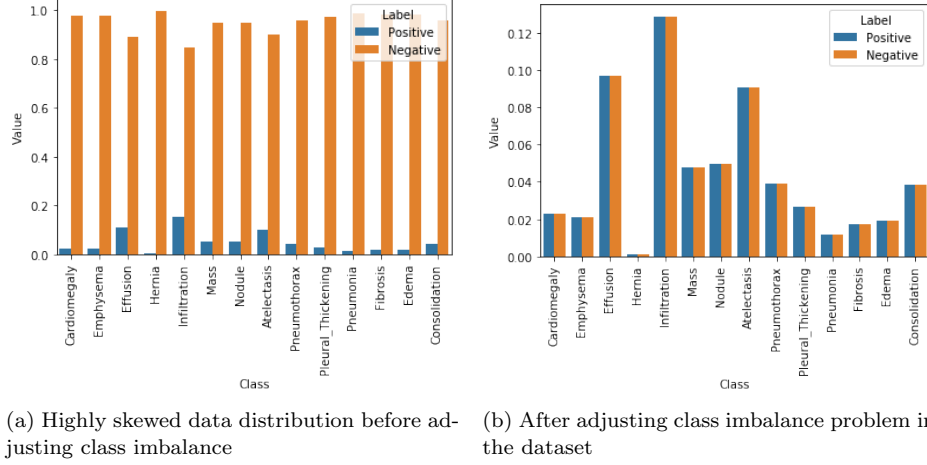


**Figure 4.** Solving class-imbalance problem

of images with disease labels to those without disease labels was only around 0.18. If a model is trained using an imbalanced dataset with a normal cross-entropy loss function, the algorithm will prioritize the majority class, leading to bias towards one type of label. To mitigate this issue, we modified our cross-entropy loss.

### 2.3. Training

The normal cross-entropy loss, which is commonly used in classification models, for the  $i^{th}$  example is given by:

$$L_{\text{cross-entropy}}(x_i) = -(y_i \log(g(x_i)) + (1 - y_i) \log(1 - g(x_i))) \quad (1)$$

Here,  $x_i$  and  $y_i$  denote the features and label of the given image, respectively, and  $g(x_i)$  represents the model prediction.

Either  $y_i$  or  $(1 - y_i)$  will contribute to the loss at any given time since, when  $y_i$  equals one,  $(1 - y_i)$  is zero and vice versa. This means that in an imbalanced dataset, one label will dominate the loss.

For an entire training set of size  $N$ , the cross-entropy loss is given by:

$$L_{\text{cross-entropy}}(D) = -(1/N) \left( \sum_{\text{positive examples}} \log(g(x_i)) + \sum_{\text{negative examples}} \log(1 - g(x_i)) \right) \quad (2)$$

Here, the first summation term represents the loss for all positive examples, while the second summation term represents the loss for all negative examples. This loss function leads to bias towards the majority class in an imbalanced dataset.

To address the problem of a highly skewed data distribution, it is crucial to ensure that each class's labels make an equal contribution. This can be achieved by multiplying each example from each class by a class-specific weight factor, denoted as  $w_{\text{pos}}$  and  $w_{\text{neg}}$ . To obtain equal contribution from both positive and negative classes, we aim to

satisfy the following condition:

$$w_{pos} \times freq_p = w_{neg} \times freq_n \quad (3)$$

For this condition to hold, we set:

$$w_{pos} = freq_{neg} \quad (4)$$

and

$$w_{neg} = freq_{pos} \quad (5)$$

Here,  $freq_p$  and  $freq_n$  represent the frequency of positive and negative examples, respectively, defined as:

$$freq_p = (\text{number of positive examples})/N \quad (6)$$

and

$$freq_n = (\text{number of negative examples})/N \quad (7)$$

After adjusting the class imbalance, the contribution of positive and negative labels to the loss function became equal, as shown in Figure 4. Therefore, the final weighted loss after computing the positive and negative weights is given by:

$$L_{cross-entropy}^w(x) = -(w_{pos}y \log(f(x)) + w_{neg}(1-y) \log(1-f(x))) \quad (8)$$

Here,  $y$  represents the true label,  $f(x)$  represents the predicted label, and  $w_{pos}$  and  $w_{neg}$  represent the class-specific weight factors for positive and negative examples, respectively.

### 2.3.1. Network Architecture

Neural networks consist of a series of layers, where each layer takes in a previous state vector  $h(n)$  and produces a new state vector,  $h(n+1) = F(h(n))$ . The function  $F$  can be an activation applied to a summation or convolutional block, or an LSTM cell. However, adding more layers does not necessarily improve the function approximation or accuracy of the network. In fact, it can decrease the accuracy of both the training and test sets due to the vanishing gradient problem.

The vanishing gradient problem arises because the gradients of the loss function slowly decrease to zero following multiple chain rules. As a result, the weights never change their values, and there is no learning in the network. This causes the accuracy to become stuck at some saturation point and degrade, which is also known as the degradation problem.

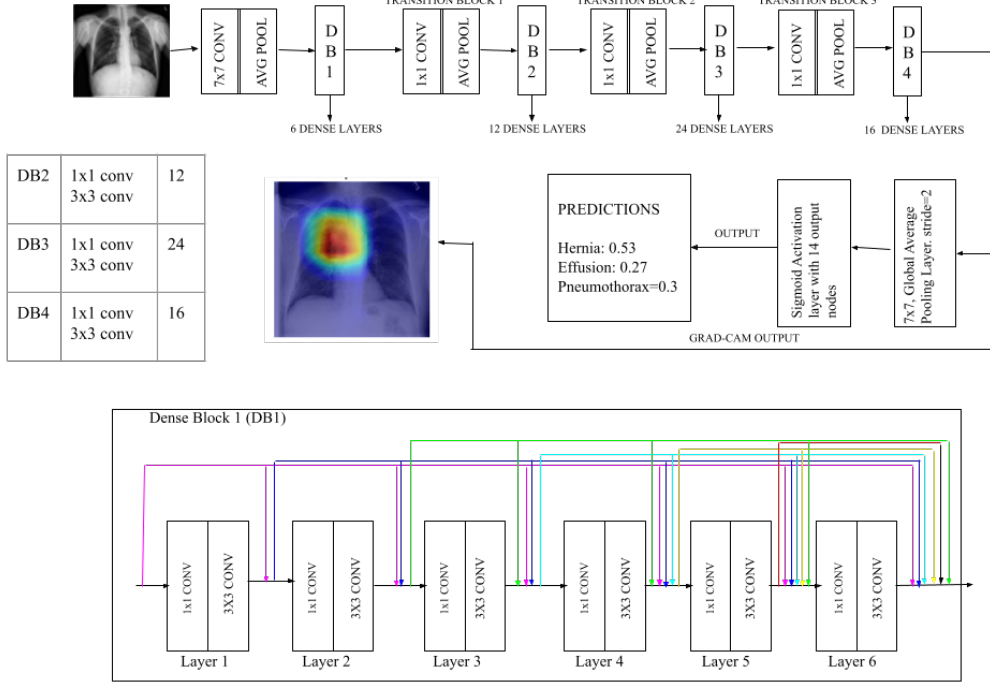


**Figure 5.** Network architecture for the proposed diagnostic model using DenseNet.

The DenseNet architecture (Huang et al. (2017)) addresses this problem by directly connecting each layer with all the other layers, allowing each individual layer to access all the earlier layers of the network. This approach ensures that the gradient signals and information can be efficiently propagated throughout the network, leading to more effective learning and better accuracy.

The DenseNet architecture is divided into two main blocks: the DenseBlock and the TransitionBlock. In a DenseBlock, the feature size dimension remains the same, but the number of filters varies. Each layer in a DenseBlock computes two convolutional operations: a 1x1 convolution, which is used for extracting features, and a 3x3 convolution, which is used for decreasing the feature depth. The TransitionBlock is present between the DenseBlocks and its main function is to downsample the feature size by applying a 1x1 convolution and a 2x2 average pooling function. This downsampling operation reduces the spatial resolution of the feature maps, which can help to reduce the computational cost and prevent overfitting. The output of the TransitionBlock is then fed into the next DenseBlock, where the process is repeated. Overall, the DenseNet architecture's unique design allows for efficient feature reuse and propagation throughout the network, leading to improved accuracy and reduced overfitting.

For our work, we utilized a DenseNet-121 architecture, which consists of 4 Dense Blocks with Dense Block 1 comprising 6 dense layers, Dense Block 2 comprising 12 dense layers, Dense Block 3 consisting of 24 dense layers, and Dense Block 4 consisting of 16 dense layers. There are 3 transition blocks between the Dense Blocks. The number 121 in DenseNet-121 refers to the total number of layers with trainable weights. We utilized transfer learning by using pre-trained weights from ImageNet as the initial weights for the architecture. The ReLU activation function was used in the hidden

layers.

The early layers of the DenseNet architecture with ImageNet weights were left unmodified as they carry general features of images, such as edges. The top layers carry information about specific features of the images, so they were skipped, and an additional two layers were added: a Global Average Pooling layer and a Dense layer with sigmoid activation. The Global Average Pooling layer was used to compute the average of the last convolution layer in the network, and the Dense Layer with sigmoid activation provided the prediction for all of the target classes.

It is important to note that the problem addressed in this project is a multi-label classification problem, where there can be more than one correct answer. Each X-ray image predicts the probability for each pathology differently, allowing each condition to have a high or low probability independent of the results of other labels. Therefore, a sigmoid function was used on each raw output independently. The loss function in this project is the weighted loss function explained by Equation 8.

After specifying the neural network architecture, the model was trained using back-propagation (LeCun et al. (1998)) with mini-batch stochastic gradient descent of 8 images and the Adam optimizer (Kingma and Ba (2015)) with a default learning rate of 0.001.

#### 2.4. Testing

We trained the model on different sizes of the training dataset with different hyper-parameters to observe the generalization accuracy of the model against an unseen test set. The test set was drawn from the same data distribution as the training data and split by patient ID to avoid data leakage.

To perform a quantitative analysis of our model, we computed the following metrics:

- (1) **Sensitivity and Specificity:** Sensitivity is defined as the probability that the model predicts that the patient has a disease given that the patient has the disease. It is also known as the True Positive Rate or Recall. On the other hand, specificity, also known as the True Negative Ratio, is defined as the probability that the model predicts that the patient is disease-free provided that the patient is normal.

$$Sensitivity = TP / (TP + FN) \quad (9)$$

$$Specificity = TN / (TN + FP) \quad (10)$$

- (2) **Positive Predictive Value and Negative Predictive Value:** Diagnostically, sensitivity and specificity are not helpful alone. While sensitivity tells the probability that the test results positive given that the person already has the condition, the information of probability that the person has the disease given that the test gives positive is important. Positive Predictive Value (PPV) also called Precision, provides the probability that a patient has the disease given that the model prediction is positive. Negative Predictive Value (NPV) provides the probability that a patient does not have a disease when the model prediction is negative.

$$PPV = TP / (TP + FP) \quad (11)$$

$$NPV = TN / (TN + FN) \quad (12)$$

Here, TP (True Positive) is the number of correctly predicted positive samples, FN (False Negative) is the number of incorrectly predicted negative samples, TN (True Negative) is the number of correctly predicted negative samples, and FP (False Positive) is the number of incorrectly predicted positive samples.

(3) **ROC curve:** A classification model predicts the True Positives and Negatives based on a threshold that dictates what output label is considered positive and negative. This threshold value can be any random number, and it should not affect the decision provided by the model. To see how the threshold affects the decision of the model, we can plot a graph of True Positive Rate vs False Positive Rate at different threshold settings to obtain the ROC curve.

The area under the ROC curve (AUC) is a measure of the goodness of fit of the model. In medical literature, this number also gives the probability that a randomly selected patient who experienced a condition had a higher risk score than a patient who had not experienced the event. A higher AUC indicates better performance of the model in distinguishing between positive and negative samples.

(4) **F1 score:** F1 score is computed by taking the harmonic mean of the precision and recall. The best value of the F1 score is 1 under the condition of perfect precision and recall, while its worst value is 0. In this project, the F1 score of each pathology detection is calculated. If a single F-score is required for multiclass classification, a micro-average (weighted by the class frequency) or macro-average (taking the same weights for all classes) approach for F1 scores can be followed.

### 3. Results

#### 3.1. Evaluation of diagnostic model

The model was initially trained on a relatively small dataset of 1000 images for five epochs and tested against a separate test set. The receiver operating characteristic (ROC) curve obtained is shown in Figure 6. The results indicate that the model performed poorly, with the curve of prediction for each pathology closely approximating the diagonal, suggesting the model was a poor classifier. The corresponding area under the ROC curve (AUC) scores further support this observation, revealing inaccurate prediction of disease by the model across different thresholds. We hypothesize that the underperformance of the model is due to underfitting and the insufficient size of the training dataset and number of training epochs. We anticipate that the performance of the model will improve significantly after training on a larger dataset with a larger number of epochs.

Table 2 presents the evaluation metrics computed on the test dataset based on the model trained on 1000 X-ray images. The results reveal that the model failed to generalize, as evidenced by poor performance across all metrics. While accuracy can be

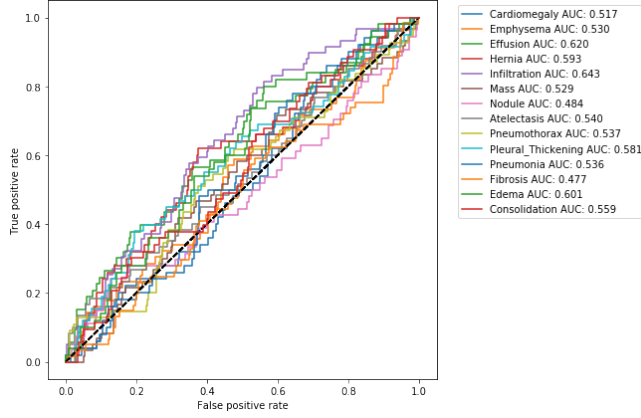


**Figure 6.** ROC curve on classification of thoracic pathologies by a model trained on small dataset of 1000 images.

**Table 2.** Table of evaluation metrics after training on 1000 images

	Accuracy	Prevalence	Sensitivity	Specificity	PPV	NPV	AUC	F1	Threshold
Cardiomegaly	0.445	0.119	0.54	0.432	0.114	0.874	0.517	0.188	0.5
Emphysema	0.864	0.133	0	0.997	0	0.866	0.53	0	0.5
Effusion	0.524	0.126	0.66	0.504	0.161	0.911	0.62	0.259	0.5
Hernia	0.881	0.119	0	1	NaN	0.881	0.593	0	0.5
Infiltration	0.54	0.14	0.712	0.512	0.193	0.916	0.643	0.303	0.5
Mass	0.167	0.143	0.9	0.044	0.136	0.727	0.529	0.236	0.5
Nodule	0.595	0.129	0.352	0.631	0.123	0.868	0.484	0.183	0.5
Atelectasis	0.41	0.143	0.65	0.369	0.147	0.864	0.54	0.239	0.5
Pneumothorax	0.869	0.131	0	1	NaN	0.869	0.537	0	0.5
Pleural_Thickening	0.862	0.138	0	1	NaN	0.862	0.581	0	0.5
Pneumonia	0.514	0.119	0.54	0.511	0.13	0.892	0.536	0.209	0.5
Fibrosis	0.855	0.145	0	1	NaN	0.855	0.477	0	0.5
Edema	0.624	0.119	0.54	0.635	0.167	0.911	0.601	0.255	0.5
Consolidation	0.65	0.126	0.377	0.689	0.149	0.885	0.559	0.214	0.5

misleading, especially in cases of Pneumothorax, Hernia, and Pleural Thickening, the corresponding F1 scores provide a more accurate estimation of generalization, which is unacceptable. Furthermore, some conditions lack precision and recall values due to zero true positives and false positives.

To address the issue of underfitting, we increased the size of the training dataset to 99,000 images while keeping the epoch number constant. However, this did not improve the generalization performance of the model, with the ROC plot in Figure 7(a) indicating a decrease in prediction accuracy. These results suggest that the model is not complex enough to capture the underlying patterns in the data.

To address the issue of underfitting, we increased the number of training epochs to 100 and implemented adaptive learning rate and dropout with a rate of 10% (Srivastava et al. (2014)). These regularization techniques were applied to prevent overfitting on the training data.

The ROC curve shown in Figure 7(b) illustrates the performance of the classifier for different pathology conditions across various thresholds. The corresponding evaluation metric table in Table 3 provides the final measures of evaluation criteria for each condition. The results demonstrate a significant improvement in the discriminative performance of the model on all conditions compared to our previous experiments. However, we note that while the model achieved high sensitivity and accuracy, the positive predictive value (PPV) of the predictions can still be low. For instance, consider the predictions of Pneumonia, which has a sensitivity of 0.6. Given that the model

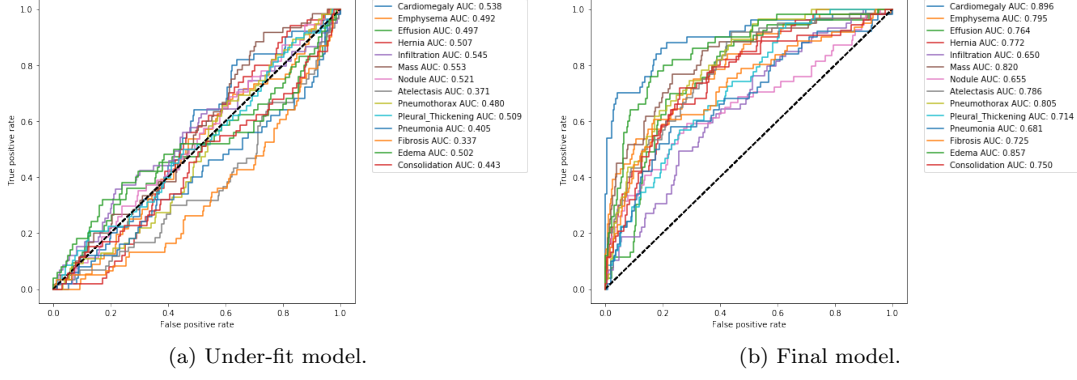


**Figure 7.** ROC curve on classification of thoracic pathologies by a model trained on complete dataset.

predicted a positive result, the probability that the person actually has Pneumonia is only 0.18. These results highlight the importance of considering both sensitivity and PPV in evaluating the performance of the model.

**Table 3.** Table of evaluation metrics after training on 99000 images with regularizer

	Accuracy	Prevalence	Sensitivity	Specificity	PPV	NPV	AUC	F1	Threshold
Cardiomegaly	0.826	0.119	0.78	0.832	0.386	0.966	0.896	0.517	0.5
Emphysema	0.762	0.133	0.589	0.788	0.3	0.926	0.795	0.398	0.5
Effusion	0.681	0.126	0.736	0.673	0.245	0.946	0.764	0.368	0.5
Hernia	0.705	0.119	0.66	0.711	0.236	0.939	0.772	0.347	0.5
Infiltration	0.598	0.14	0.644	0.59	0.204	0.91	0.65	0.31	0.5
Mass	0.764	0.143	0.75	0.767	0.349	0.948	0.82	0.476	0.5
Nodule	0.66	0.129	0.593	0.669	0.209	0.918	0.655	0.309	0.5
Atelectasis	0.674	0.143	0.75	0.661	0.269	0.941	0.786	0.396	0.5
Pneumothorax	0.7	0.131	0.745	0.693	0.268	0.948	0.805	0.394	0.5
Pleural_Thickening	0.6	0.138	0.672	0.588	0.207	0.918	0.714	0.317	0.5
Pneumonia	0.633	0.119	0.6	0.638	0.183	0.922	0.681	0.28	0.5
Fibrosis	0.65	0.145	0.623	0.655	0.235	0.911	0.725	0.341	0.5
Edema	0.783	0.119	0.8	0.781	0.331	0.967	0.857	0.468	0.5
Consolidation	0.607	0.126	0.792	0.58	0.214	0.951	0.75	0.337	0.5

In Table 4, we compare the performance of our proposed architecture against CheXNext (Rajpurkar et al. (2018)) on selected predictions. The results demonstrate that our proposed architecture outperforms CheXNext in detecting cardiomegaly, a condition characterized by abnormal enlargement of the heart. In contrast, the performance of our proposed architecture is comparable to that of CheXNext on other predictions.

**Table 4.** Comparing performance of the proposed architecture.

Pathology	This project	CheXNext (Rajpurkar et al. (2018))
Cardiomegaly	0.896	0.831
Edema	0.857	0.924
Mass	0.82	0.909
Effusion	0.764	0.901
Consolidation	0.75	0.893
Pneumothorax	0.805	0.944
Pneumonia	0.681	0.851

### 3.2. Model interpretation

Interpreting deep learning models is a challenging task due to their complex architecture (Ribeiro et al. (2016)). Class Activation Maps (CAMs) (Kwaśniewska et al. (2017)) are a popular method for generating test case explanations of model predictions for convolutional neural networks (CNNs). CAMs enable us to understand where the deep learning model is focusing its attention when making a classification. To generate heat-maps for highlighting the important regions in X-rays during prediction, we employed GRADCAM (Selvaraju et al. (2017)). While GRADCAM does not provide detailed information for the reasoning behind our model predictions, it can still be useful for expert validation to confirm whether the model is focusing on the appropriate regions in the image to make associated predictions.

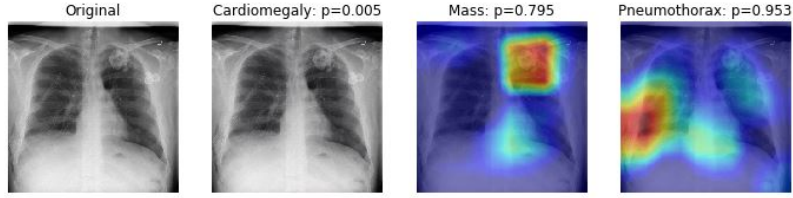


**Figure 8.** Visualization of pathology prediction using GRADCAM

In Figure 8, we present the visualization of our learning using GRADCAM. We generated heat-maps for two classes with the highest performing AUC measures and one with the lowest AUC measure. As shown in the figure, the activation map generates a heatmap that highlights the region that was attended to by the model when making predictions for Mass and Pneumothorax. In contrast, since the prediction of Cardiomegaly was very low, no heatmap is produced on the X-ray image as the model did not identify any region to make a correct decision. These findings demonstrate the potential utility of CAMs in helping experts to validate the performance of the model and to gain insights into the model’s decision-making process.

### 3.3. Uncertainty estimation

Computing the confidence interval of our measurement enables us to understand how the measurement is affected by sampling, providing an estimation of uncertainty that quantifies how confident we are in our predictions based on the training dataset, which is only a sample of the real-world data. In this experiment, we computed the confidence interval of the AUC score and obtained the results, as shown in Table 5. These findings provide valuable insights into the reliability of our model predictions and confirm that regardless of sampling, our proposed approach will produce similar results.

We observe that, our confidence intervals are narrower for almost all classes. Predictions with narrow interval shows confidence in the result and regardless of the sampling, our experiment will produce similar results.

## 4. Discussion

In this work, we developed a disease diagnosis model for detecting thoracic diseases and provided extensive evaluation to demonstrate the effectiveness of deep neural

**Table 5.** Table of confidence interval for AUC score.

Pathology	Mean AUC (CI 5%-95%)
Cardiomegaly	0.89 (0.86-0.92)
Emphysema	0.79 (0.76-0.82)
Effusion	0.76 (0.73-0.80)
Hernia	0.77 (0.73-0.80)
Infiltration	0.65 (0.62-0.68)
Mass	0.82 (0.79-0.85)
Nodule	0.65 (0.60-0.70)
Atelectasis	0.79 (0.76-0.81)
Pneumothorax	0.81 (0.77-0.83)
Pleural_Thickening	0.71 (0.68-0.74)
Pneumonia	0.68 (0.62-0.73)
Fibrosis	0.72 (0.68-0.76)
Edema	0.86 (0.82-0.88)
Consolidation	0.75 (0.72-0.78)

network-based models in disease diagnosis, provided they have model interpretability to assist decision-making. However, this work also has several limitations. The primary limitation of this deep learning model is that it was trained using only frontal X-rays. Due to the unavailability of other types of images, we could only use one type of X-ray to train the model. Incorporating both front and lateral radiology images could improve the model's performance on most practical cases. Additionally, the model does not consider the patient's medical history, which is critical in disease diagnosis. However, we focused solely on using images as a factor for determining whether a patient has a thoracic disease or not. Finally, the model was trained on a subset of the total available images due to computational constraints. Despite these limitations, our work provides promising results that can inform the development of future disease diagnosis models.

## 5. Conclusion

Chest X-rays remain one of the most common diagnostic tools for the detection of various thoracic diseases. However, a large portion of the global population still lacks access to even the most basic forms of radiology diagnosis. The results of this work underscore the need for the implementation of an automated diagnosis system for the detection of thoracic diseases, with the ability to interpret the results of the deep learning model. The next step in this research is to collaborate with healthcare professionals to compare model predictions with their decisions and evaluate how well the deep learning model functions compared to doctors. Professional input can also help improve the model's performance and interpretation. By working together, we can pave the way for the development of more accurate and accessible disease diagnostic tools, ultimately improving health outcomes for patients worldwide.

### *Data Availability*

The dataset is publicly available at NIHCC website<sup>2</sup>.

<sup>2</sup><https://nihcc.app.box.com/v/ChestXray-NIHCC>

## ***Funding***

No funding was received to assist with the research work or preparation of this manuscript.

## ***Conflict of interest***

The authors have no competing interests to declare that are relevant to the content of this article.

## ***Ethical approval***

This article does not contain any studies with human participants performed by any of the authors. The article uses open-source datasets.

## **References**

Bar Y, Diamant I, Wolf L, Lieberman S, Konen E, Greenspan H. 2015. Chest pathology detection using deep learning with non-medical training. In: 2015 IEEE 12th international symposium on biomedical imaging (ISBI). IEEE. p. 294–297.

Cicero M, Bilbily A, Colak E, Dowdell T, Gray B, Perampaladas K, Barfett J. 2017. Training and validating a deep convolutional neural network for computer-aided detection and classification of abnormalities on frontal chest radiographs. *Investigative radiology*. 52(5):281–287.

Donahue J, Jia Y, Vinyals O, Hoffman J, Zhang N, Tzeng E, Darrell T. 2014. Decaf: A deep convolutional activation feature for generic visual recognition. In: International conference on machine learning. PMLR. p. 647–655.

Fukushima K, Wake N. 1991. Handwritten alphanumeric character recognition by the neocognitron. *IEEE transactions on Neural Networks*. 2(3):355–365.

Goodfellow I, Bengio Y, Courville A. 2016. Deep learning. MIT press.

He K, Zhang X, Ren S, Sun J. 2016. Deep residual learning for image recognition. In: Proceedings of the IEEE conference on computer vision and pattern recognition. p. 770–778.

Huang G, Liu Z, Van Der Maaten L, Weinberger KQ. 2017. Densely connected convolutional networks. In: Proceedings of the IEEE conference on computer vision and pattern recognition. p. 4700–4708.

Kingma DP, Ba J. 2015. Adam: A method for stochastic optimization. ICLR.

Krizhevsky A, Sutskever I, Hinton GE. 2012. Imagenet classification with deep convolutional neural networks. In: Pereira F, Burges CJC, Bottou L, Weinberger KQ, editors. *Advances in Neural Information Processing Systems*; vol. 25. Curran Associates, Inc.

Kwaśniewska A, Rumiński J, Rad P. 2017. Deep features class activation map for thermal face detection and tracking. In: 2017 10Th international conference on human system interactions (HSI). IEEE. p. 41–47.

Lakhani P, Sundaram B. 2017. Deep learning at chest radiography: automated classification of pulmonary tuberculosis by using convolutional neural networks. *Radiology*. 284(2):574–582.

LeCun Y, Bottou L, Bengio Y, Haffner P. 1998. Gradient-based learning applied to document recognition. *Proceedings of the IEEE*. 86(11):2278–2324.

Li Y, Shen L. 2018. Skin lesion analysis towards melanoma detection using deep learning network. *Sensors*. 18(2):556.

Litjens G, Kooi T, Bejnordi BE, Setio AAA, Ciompi F, Ghafoorian M, Van Der Laak JA, Van Ginneken B, Sánchez CI. 2017. A survey on deep learning in medical image analysis. *Medical image analysis*. 42:60–88.

Maduskar P, Muyoyeta M, Ayles H, Hogeweg L, Peters-Bax L, Van Ginneken B. 2013. Detection of tuberculosis using digital chest radiography: automated reading vs. interpretation

by clinical officers. *The International journal of tuberculosis and lung disease*. 17(12):1613–1620.

Rajpurkar P, Irvin J, Ball RL, Zhu K, Yang B, Mehta H, Duan T, Ding D, Bagul A, Langlotz CP. 2018. Deep learning for chest radiograph diagnosis: A retrospective comparison of the chexnext algorithm to practicing radiologists. *PLoS medicine*. 15(11):e1002686.

Rajpurkar P, Irvin J, Zhu K, Yang B, Mehta H, Duan T, Ding D, Bagul A, Langlotz C, Shpanskaya. 2017. Chexnet: Radiologist-level pneumonia detection on chest x-rays with deep learning. *arXiv preprint arXiv:171105225*.

Rathore S, Habes M, Iftikhar MA, Shacklett A, Davatzikos C. 2017. A review on neuroimaging-based classification studies and associated feature extraction methods for alzheimer's disease and its prodromal stages. *NeuroImage*. 155:530–548.

Ren S, He K, Girshick R, Sun J. 2015. Faster r-cnn: Towards real-time object detection with region proposal networks. *Advances in neural information processing systems*. 28:91–99.

Ribeiro MT, Singh S, Guestrin C. 2016. " why should i trust you?" explaining the predictions of any classifier. In: *Proceedings of the 22nd ACM SIGKDD international conference on knowledge discovery and data mining*. p. 1135–1144.

Selvaraju RR, Cogswell M, Das A, Vedantam R, Parikh D, Batra D. 2017. Grad-cam: Visual explanations from deep networks via gradient-based localization. In: *Proceedings of the IEEE international conference on computer vision*. p. 618–626.

Simonyan K, Zisserman A. 2015. Very deep convolutional networks for large-scale image recognition. *ICLR*.

Srivastava N, Hinton G, Krizhevsky A, Sutskever I, Salakhutdinov R. 2014. Dropout: a simple way to prevent neural networks from overfitting. *The journal of machine learning research*. 15(1):1929–1958.

Szegedy C, Ioffe S, Vanhoucke V, Alemi AA. 2017. Inception-v4, inception-resnet and the impact of residual connections on learning. In: *Thirty-first AAAI conference on artificial intelligence*.

Szegedy C, Liu W, Jia Y, Sermanet P, Reed S, Anguelov D, Erhan D, Vanhoucke V, Rabinovich A. 2015. Going deeper with convolutions. In: *Proceedings of the IEEE conference on computer vision and pattern recognition*. p. 1–9.

Tymchenko B, Marchenko P, Spodarets D. 2020. Deep learning approach to diabetic retinopathy detection. *arXiv preprint arXiv:200302261*.

Wang X, Peng Y, Lu L, Lu Z, Bagheri M, Summers RM. 2017. Chestx-ray8: Hospital-scale chest x-ray database and benchmarks on weakly-supervised classification and localization of common thorax diseases. In: *Proceedings of the IEEE conference on computer vision and pattern recognition*. p. 2097–2106.